

Submitted to ApJ

# X-ray Hardness Evolution in GRB Afterglows and Flares: Late Time GRB Activity Without $N_H$ Variations

Nathaniel R. Butler<sup>1,2</sup> and Daniel Kocevski<sup>2</sup>

## ABSTRACT

We show that the X-ray and  $\gamma$ -ray spectra of Swift GRBs and their afterglows are consistent with the emission characteristic of an expanding, relativistic fireball. The classical afterglow due to the impact of the fireball on the external medium is often not observed until one to several hours after the GRB. Focusing on GRBs 061121, 060614, and 060124, but generalizing to the full ( $>50$  Msec XRT exposure) Swift sample up to and including GRB 061210, we show that the early emission in  $>90\%$  of early afterglows has a characteristic  $\nu F_\nu$  spectral energy  $E_{\text{peak}}$  which likely evolves from the  $\gamma$ -rays through the soft X-ray band on timescales of  $10^2 - 10^4$  s after the GRB. The observed spectra are strongly curved when plotted with logarithmic axes and have often been incorrectly fitted in other studies with a time-varying soft X-ray absorption. The spectral evolution inferred from fitting instead models used to fit GRBs demonstrates a common evolution—a powerlaw hardness intensity correlation and hard to soft evolution—for GRBs and the early X-ray afterglows and X-ray flares. Combined with studies of short timescale variability, our findings indicate a central engine active for longer than previously suspected. The GRB spectra are observed to become very soft at late times due to an intrinsic spectral evolution and due to the surprising faintness of some afterglows. We discuss models for the early X-ray emission.

*Subject headings:* gamma rays: bursts — supernovae: general — X-rays: general

---

<sup>1</sup>Townes Fellow, Space Sciences Laboratory, University of California, Berkeley, CA, 94720-7450, USA

<sup>2</sup>Astronomy Department, University of California, 445 Campbell Hall, Berkeley, CA 94720-3411, USA

## 1. Introduction

The Swift satellite (Gehrels et al. 2004) and its X-ray telescope (Burrows et al. 2005b) have opened a new window into the early lives of  $\gamma$ -ray Bursts (GRBs) and their afterglows. We see a complex array of behaviors, many of which appear to directly conflict (e.g., O’Brien et al. 2006; Panaiteescu et al. 2006; Willingale et al. 2006) the well tested internal–external shock GRB and afterglow model (Rees & Mészáros 1994; Sari & Piran 1997; Sari, Piran, & Narayan 1998; Wijers & Galama 1999). In this “fireball” model, the GRB is produced via collisions of shells in a relativistic outflow, and an afterglow arises later as the ejecta sweep up and heat the surrounding medium. The Swift afterglows exhibit dramatic flaring, rapidly decaying prompt emission tails, and typically a broad plateau phase until  $t \approx 10^4$  s (e.g. Nousek et al. 2006). Early afterglow observations prior to Swift (e.g., Frontera et al. 2000) suggested instead a  $\sim 10$  s duration burst rapidly gone and replaced by the fading afterglow emission. How these observations are to be reconciled and what mechanisms produce the early afterglow emission are key open questions.

Particularly intriguing, several recent studies fit the *Swift* X-ray Telescope (XRT) data and infer a time variable soft X-ray absorption (Starling et al. 2005; Rol et al. 2006; Campana et al. 2006c). This would imply that the early afterglow is stripping electrons from a dense shell of light-element-rich material located  $R \lesssim 1$  pc from the GRB, which was not already fully ionized by the GRB. It is difficult to detect such an effect because of the strong spectral evolution common in the early afterglows (e.g., Vaughan et al. 2006; Butler 2007a, “Paper I”). A changing column density  $N_H$  cannot easily be separated from intrinsic afterglow spectral evolution, given the narrow XRT bandpass. If the early X-ray spectra exhibit log-log curvature like that of GRBs, which have  $\nu F_\nu$  spectral turnovers at a characteristic energy  $E_{\text{peak}}$  (e.g., Preece et al. 2000; Kaneko et al. 2006), then evolution in the curvature could be mistaken for variations in  $N_H$ .

As we discuss below, plots of early XRT spectra do show strong log-log curvature and an inferred  $E_{\text{peak}}$  which typically passes in time through the X-ray band. This produces a changing X-ray hardness, which we observe to correlate with the flux. A close analogy can be found in the spectral evolution of GRBs observed by the Burst and Transient Source Experiment (BATSE; Fishman et al. 1999). A characteristic feature of these spectra and light curves is a hard-to-soft evolution in time and a powerlaw hardness–intensity correlation (Golenetskii et al. 1983; Kargatis et al. 1995; Norris et al. 1996; Fenimore et al. 1995; Fenimore, Madras, & Nayakshin 1996). The recent refined study of Borgonovo & Ryde (2001) measures a powerlaw relation between the characteristic energy  $E_{\text{peak}}$  and the bolometric flux  $F_{\text{bol}}$  valid for  $>57\%$  of GRB pulses,  $E_{\text{peak}} \propto F_{\text{bol}}^{0.5 \pm 0.2}$ . We observe a consistent correlation in the soft, early-time XRT data.

In Paper I, we present evidence for this outlier population of extremely soft afterglows in the first year of *Swift* XRT afterglow data. Although they were identified via an automated search for spectral lines, the spectra are also fitted well by models containing multiple continuum components. Below and in Butler & Kocevski (2007), we explore further the phenomenology associated with this soft emission. We demonstrate that GRB-like behavior is present in the first  $t \lesssim 1$  hour of  $>90\%$  of the afterglows and is especially prominent during the flaring. In two cases, thanks to Burst Alert Telescope (BAT) triggers on bright precursors, X-ray emission coincident in time with the classical GRB is detected and can be shown to have quite similar properties to the highly time-variable emission at later times. This is strong evidence—to be combined with the short timescale variability studies (e.g., Burrows et al. 2005a; Falcone et al. 2006; Romano et al. 2006a; Pagani et al. 2006; Kocevski & Butler 2007)—tying the flare and early afterglow emission to the GRB central engine.

## 2. Data Reduction

Our automated pipeline at U. C. Berkeley downloads the *Swift* data in near real time from the *Swift* Archive<sup>1</sup> and quicklook site. We use the calibration files from the 2006-04-27 BAT and XRT database release. The additional automated processing described below is done uniformly for all afterglows via custom IDL scripts. The final data products are available for general consumption<sup>2</sup>.

The XRT suffers from a significant number of bad or unstable pixels and columns. Two central detector columns were lost due to a micro-meteorite strike<sup>3</sup>. For the early afterglows ( $t \lesssim 10^3$ s), when the satellite initially points the XRT at the source without the precise localization information needed to offset from the bad columns, a large and time-dependent fraction of the flux can be lost. In order to produce accurate light curves and properly normalized spectra, it is necessary to accurately determine the position centroid and to precisely track the loss of source and background flux due to the bad detector elements on short ( $\sim$  few second) timescales.

---

<sup>1</sup><ftp://legacy.gsfc.nasa.gov/swift/data>

<sup>2</sup><http://astro.berkeley.edu/~nat/swift>

<sup>3</sup>[http://swift.gsfc.nasa.gov/docs/heasarc/caldb/swift/docs/xrt/SWIFT-XRT-CALDB-01\\_v5.pdf](http://swift.gsfc.nasa.gov/docs/heasarc/caldb/swift/docs/xrt/SWIFT-XRT-CALDB-01_v5.pdf)

## 2.1. Photon Counting (PC) Mode Light Curves

We begin by projecting the data in the 0.5-8.0 keV band from each PC mode followup observation onto a tangent plane centered at the source position quoted by the XRT Team. In raw coordinates, we reject all pixels with more than six counts and also containing more signal than contained in the surrounding 8 pixels summed. Using the aspect solution file (`*sat*.fits`), we determine the satellite pointing for each detection frame. We then map the bad pixels in raw detector coordinates determined by `xrtpipeline` and by our algorithm onto the sky on a frame-by-frame basis. This is used to generate exposure maps for the full observation and as a function of time.

Using the full exposure map, we determine the afterglow position centroid (see, Butler 2007b) to fix the source extraction region. We consider a 16 pixel radius source extraction region, surrounding by an annular background extraction region of outer radius 64 pixels. Running `wavdetect` (see, Butler 2007b), we then determine the positions of field sources in the image. We mask out the regions corresponding to the field sources from the source and background extraction regions. Also, using the Point Spread Function (PSF) model (`swxpsf20010101v003.fits`) at 1.3 keV, we determine the level of residual field source contamination in the source extraction region (typically negligible) for later subtraction.

Initially ignoring pileup, we extract the source and background counts for each good time interval of data acquisition. The fraction of lost signal and the scale factor relating the background in the source and background extraction regions is determined for each extraction using the time-dependent exposure map. assuming these exposure corrections for the entirety of each time interval, we subdivide the counts in each interval so that a fixed signal-to-noise of 3 is achieved.

In order to check and to account for pileup, we perform a coarse Bayesian blocking (Scargle 1998), with a strong prior weight against adding a new segment ( $e^{-50}$ ). Using the maximum observed count rate in each segment thus determined, we find the minimum aperture necessary to reduce the source signal to levels where pileup is negligible. The coarse blocking results in a small number of regions (typically 2–3) of differing inner extraction radius for an afterglow. We assume pileup is important for count rates  $> 0.5$  cps (see also, Nousek et al. 2006). The light curves are verified to transition smoothly across regions of different inner extraction region radius. Using the time intervals and pileup corrected apertures thus determined, we rebin the data to a signal-to-noise of 3 and recalculate the exposure correction for each time interval. The final time regions and exposure corrections define our temporal extractions regions for the extraction of light curves in different energy bands and for extraction of spectra below.

## 2.2. Windowed Timing (WT) Mode Light Curves

Our reduction of the WT mode data closely parallels our PC mode reduction, except that it is more natural to extract the WT mode data in raw detector coordinates than in sky coordinates as done above for the PC mode data. This is due to the readout mode; detector pixels are summed in RAW-Y and the resulting data are in column (RAW-X) format.

Summing the data from each WT mode followup, we reject any RAW-X columns containing a  $> 10\sigma$  count rate relative to the background, after first ignoring pixels in the 16 pixel source extraction region. We also reject any RAW-X columns containing 100 times more signal than the highest neighboring column (or  $> 100$  if the neighbors contain no signal). Using the sky image determined from the PC mode data and the satellite aspect, we project the background onto the RAW-X axis and form a background mask for the 64 pixel outer radius and 16 pixel inner radius extraction region. We do not allow masking of the pixels within the central 16 pixel source regions. If the source is bright ( $> 10^3$  cps), we recenter the source and background apertures. Small aspect shifts  $\sim 1$  pixel are not uncommon between the PC and WT mode data and must be accounted for.

We determine the exposure corrections as for the PC mode data, but also adjusting the PSF model for the WT mode summing of RAW-Y pixels. We note that our exposure corrections account for source signal contained in the background region. We determine a pileup correction as above, but with a limiting source count rate of 150 cps (see also, Nousek et al. 2006).

## 2.3. PC and WT Mode Spectra

Spectral response files are generated using the `xrtmkarf` task for each time interval of interest. Our invocation of the task ignores the exposure maps calculated above, determining the energy dependence of the source extraction assuming only the inner and outer source and background regions. We then adjust the normalization of the resulting Ancillary Response File (ARF) to account for the actual loss in flux (0.5-8.0 keV) on a pixel by pixel basis using the divided time intervals and associated exposure corrections determined above. The spectra are fit in ISIS<sup>4</sup>. For each spectral bin, we require a S/N of 3.5. We define S/N as the background-subtracted number of counts divided by the square root of the sum of the signal counts and the variance in the background. As done in Paper I, we restrict our attention to time-resolved spectra containing 500 or more counts or to spectra formed by

---

<sup>4</sup><http://space.mit.edu/CXC/ISIS/>

grouping two or more of the 500 counts spectra.

We fit the PC and WT mode data over the 0.3-10.0 keV range, also accounting for the systematic calibration uncertainties  $\sim 3\%$ <sup>5</sup>. In WT mode, we allow the detector gain to vary by  $\pm 80$  eV<sup>6</sup>.

## 2.4. BAT Light Curves and Spectra

We establish the energy scale and mask weighting for the BAT data by running the `bateconvert` and `batmaskwtevt` tasks. The mask-weighting removes flux from background sources. Spectra and light curves are extracted with the `batbinevt` task, and response matrices are produced by running `batdrmgen`. We apply the systematic error corrections to the low-energy BAT spectral data as suggested by the BAT Digest website<sup>7</sup>, and fit the data using ISIS. The spectral normalizations are corrected for satellite slews using the `batupdatephakw` task. For GRB 060124 below, BAT spectral fits are performed on the mask tagged light curve data in four channels, assuming the on-axis response and also accounting for the systematic error.

## 3. The Joint BAT+XRT Spectra of Three Events

There are two bright events in the XRT sample which overlap in time entirely with what would commonly be thought of as the prompt phase of GRB emission. The observations by the XRT were made possible by a bright precursor just minutes prior to each GRB observed in the BAT, on which the BAT triggered. We therefore have both BAT and XRT data for each event, GRB 060124 and GRB 061121. We also discuss the bright event GRB 060614, which has excellent XRT coverage due to an early, rapid spacecraft slew.

Figure 1 displays spectral fits to a selected set of time-resolved intervals in each events. The best-fit model parameters are given in Table 1. The time evolution of these parameters are presented and discussed in detail in the next three subsections.

---

<sup>5</sup>[http://swift.gsfc.nasa.gov/docs/heasarc/caldb/swift/docs/xrt/spie05\\_romano.pdf](http://swift.gsfc.nasa.gov/docs/heasarc/caldb/swift/docs/xrt/spie05_romano.pdf)

<sup>6</sup>[http://swift.gsfc.nasa.gov/docs/heasarc/caldb/swift/docs/xrt/xrt\\_bias.pdf](http://swift.gsfc.nasa.gov/docs/heasarc/caldb/swift/docs/xrt/xrt_bias.pdf)

<sup>7</sup>[http://swift.gsfc.nasa.gov/docs/swift/analysis/bat\\_digest.html](http://swift.gsfc.nasa.gov/docs/swift/analysis/bat_digest.html)

### 3.1. GRB 060124

Swift-BAT triggered and located the precursor to GRB 060124, allowing the XRT to slew and begin simultaneous observations 106s later (Holland et al. 2006). This event is also discussed in Romano et al. (2006b). The 0.3–10.0 keV light curve is plotted in Figure 2. There are two prominent peaks. As shown in the background (lighter two shades of gray), the time profile in the soft XRT channel (0.3–1.3 keV) is broader than that in the hard channel (1.3–10.0 keV). The BAT light curve shows even narrower time structure and resolves the broad first XRT peak into at least 3 sub-peaks. The light curve after the flare ( $t > 10^4$ s) and extending to 22 days is well fit by a powerlaw  $t^{-1.32 \pm 0.01}$  ( $\chi^2/\nu = 535.2/465$ ).

We group the XRT data into  $\gtrsim 500$  counts spectra and fit powerlaws (Figure 3, left). Each fit is statistically acceptable, with a reduced  $\chi^2$  of order unity. The photon index  $\Gamma$  is observed to decrease in time, although with modulation in time that correlates with the X-ray flux and with  $N_H$  (see explanation in Section 5.1). At late times ( $t > 10^4$ s), the  $N_H$  values asymptote to the blue, dashed curve ( $N_H = 2.3 \pm 0.2 \times 10^{21}$  cm $^{-2}$ ) plotted in the figure.

To study the time varying log-log curvature, we jointly fit the BAT and XRT data using the Band et al. (1993) model. Here, we choose extraction regions which allow for a BAT signal-to-noise of 20 or higher. We also fix the column density  $N_H$  to the late time value. The model fit is actually a progression of fits of nested models (e.g., Protassov et al. 2002), from the simplest powerlaw model to a powerlaw times exponential model, to the smoothly broken powerlaw Band model. Each more complex model has one additional degree of freedom. We accept or reject the more complex model at each stage by requiring  $\Delta\chi^2 > 2.706$  (i.e., 90% confidence). If the data are acceptably fit by only the powerlaw model, we quote a limit on  $E_{\text{peak}}$  using either the exponential times powerlaw model (for  $\Gamma < 2$ ) or the constrained Band formalism (Sakamoto et al. 2003, ; for  $\Gamma > 2$ ). In order that  $E_{\text{peak}}$  correspond to a peak in the  $\nu F_\nu$  spectrum, we require the low energy index  $\alpha > -2$  and the high energy index  $\beta < -2$ . After finding that the fits were consistent with  $\alpha < 0$ , as also found for *BATSE* GRBs (Preece et al. 2000; Kaneko et al. 2006), we included this as a constraint to derive the tightest error bounds on the other model parameters.

As shown in Figure 3 (right), the data are better fit ( $> 90\%$  confidence) with the Band model in most of the time regions. The peak energy rises and declines with each of the four prominent light curve pulses. For each pulse, we present powerlaw fits to the  $E_{\text{peak}}$  declines. The rises are not well measured, as is also typically the case for *BATSE* bursts (e.g., Kocevski, Ryde, & Liang 2003). Prior to  $t \lesssim 800$ s, the observed spectrum corresponds mostly to the low energy portion of the Band model spectrum, except episodically at the flare troughs, where  $E_{\text{peak}}$  enters the X-ray band. These times regions are also those of

highest  $N_H$  in Figure 3 (left). The third pulse decline exhibits a strong evolution in both  $\alpha$  and  $E_{\text{peak}}$ . After  $t \sim 800\text{s}$  the observed spectrum corresponds to the high energy portion of the model spectrum, and  $E_{\text{peak}}$  has transited the X-ray band. Figure 1 (middle) plots the  $\nu F_\nu$  spectrum at 3 time epochs.

Motivated by the watershed event GRB 060218 (Paper I; Campana et al. 2006a), we also attempt to fit the X-ray curvature using a powerlaw plus blackbody model. The fits to the X-ray data alone are provocative and show a smooth temperature decline after each of the two major pulses. However, the fits are statistically unacceptable when we also attempt to account for the BAT data. This is also true for the GRB 061121 spectra discussed in the next sub-section. This should be taken as a caveat also to the powerlaw plus blackbody fits presented for the XRT data in Paper I, where the derived blackbody temperature variation may imply instead to  $E_{\text{peak}}$  variations. We note, however, that the X-ray spectra of the unusual GRB 060218 burst and afterglow are better fit by a blackbody plus powerlaw than by a Band model (Paper I). We do not consider the possibility of two powerlaws and a blackbody for the bursts discussed here.

### 3.2. GRB 061121

*Swift*-BAT triggered on and began observing the precursor to GRB 061121 55s prior to the XRT slew toward and onset of the main GRB event (Page et al. 2006). The *Swift* team designated this event a “Burst of Interest” (Gehrels et al. 2006) due to the rare simultaneous detections in the BAT and XRT bands and at longer wavelengths. As shown in Figure 4, the  $\gamma$ -ray and X-ray light curves show multiple peaks, with most of the prominent time structure apparent in only the  $\gamma$ -ray band.

In Figures 3 (top), we show the results of powerlaw and Band model fits to the 061121 data. The data are not of as high signal-to-noise in the X-ray band as the 060124 data, however, many of the same trends are apparent. There is a hard to soft evolution apparent in the powerlaw photon index and a correlation between the photon index and  $N_H$ . The Band model photon index goes from the low energy side to the high energy once  $E_{\text{peak}}$  has crossed the X-ray band.  $E_{\text{peak}}$  also appears to rise and fall with flaring prior to 80s. The  $\nu F_\nu$  spectrum is plotted at two epoch in Figure 1 (top). For the Band fits, we use the late time ( $t > 10^4\text{s}$ )  $N_H = 2.5 \pm 0.3 \times 10^{21} \text{ cm}^{-2}$ .

*XMM* data for this event beginning after  $t \approx 6\text{hrs}$  show consistent powerlaw fits with our late-time fits (Butler et al. 2007). In particular,  $N_H = 1.71_{-0.02}^{+0.03} \times 10^{21} \text{ cm}^{-2}$ , consistent with our late-time  $N_H$  at the  $2\sigma$  level and well below the mean early-time value. *XMM* and XRT

data generally agree well with respect to the late-time  $N_H$  determinations (e.g., Moretti et al. 2006).

### 3.3. GRB 060614

The GRB 060614 (Parsons et al. 2006) afterglow fades rapidly as a powerlaw from the prompt emission, with no flaring (Figure 5). There is excellent BAT+XRT coverage during the prompt tail emission lasting to  $t \sim 150$ s. We observe weak  $N_H$ – $\Gamma$  correlated modulations during the rapidly fading tail, which would imply an  $N_H$  that decreases in time, reaching the value marked by the dashed line in Figure 3 (left) by  $t = 10^4$ s.

However, the Band model fits show an  $E_{\text{peak}}$  which passes through the X-ray band without requiring a varying  $N_H$ . Extrapolating backward through the prompt emission, the best fit decay also fits two  $E_{\text{peak}}$  limits derived for the BAT only prompt emission. Figure 1 (bottom) plots the  $\nu F_\nu$  spectrum at two epochs. Expressed in terms of the flux  $F_{\text{XRT}}$  as measured by the XRT rate,  $E_{\text{peak}} \propto F_{\text{XRT}}^{-0.72 \pm 0.03}$ .

The low-energy photon index  $\alpha$  also appears to evolve in time after the main GRB emission.

### 3.4. Hardness Plots for GRBs 061121, 060124 and 060614

It will be useful below to see how the spectral evolution in the early X-ray light curves of GRBs 061121, 060124 and 060614 impacts the X-ray hardness ratio. We define this is the ratio of counts in the 1.3–10.0 keV band to the counts in the 0.1–1.3 keV band. The average hardness ratio ( $HR$ ) for most afterglows is 1.

Figure 6 in 9 panels shows the hardness and rate time profiles for GRBs 061121, 060124, 060614. The middle panels (looking top to bottom) show the X-ray light curve fit using an extension of the Bayesian blocks algorithm (Scargle 1998) to piecewise logarithmic data. The rate and hardness data are fit jointly, allowing the minimum number of powerlaw segments such that  $\chi^2/\nu \sim 1$ . The fits to the rate and hardness are plotted in the top and middle panels, indexed according to time. The hardness tracks the flux and moves along roughly parallel tracks. In the bottom panels, the flux in both XRT bands (top panel) and the hardness (bottom panel) are plotted for each powerlaw segment. During the decline phase of each pulse, the hardness scales as the square-root of the rate for GRBs 061121 and 060124. For the GRB 060614, the hardness and flux track as found above for  $E_{\text{peak}}$  and flux.

Each pulse in GRB 060124 peaks at roughly the same time, independent of energy band. There is, however, a hardness rise during the flux rise because the hard band increases more rapidly. There is also a modest overall hard to soft trend throughout the light curve.

The hardness plot does not capture the strong spectral variations between 500 and 600s in GRB 060124, which are apparent from the broad band fits (Figure 3 middle) and occur mostly for  $E_{\text{peak}}$  above the XRT bandpass. The time dependences of  $E_{\text{peak}}$  during this region and later are given in the figure. The  $E_{\text{peak}}$  dependence can also be given in terms of the flux  $F$ , in order to sidestep the problem of unknown start time. For all but the last flare, where we use the XRT count rate, we use the BAT 15–350 keV count rate for the flux. For pulses 1–4, we find  $E_{\text{peak}} \propto F_{\text{BAT}}^{-3.6 \pm 1.7}$ ,  $F_{\text{BAT}}^{-1.8 \pm 0.5}$ ,  $F_{\text{BAT}}^{-0.3 \pm 0.1}$ ,  $F_{\text{XRT}}^{-1.2 \pm 0.2}$ . In the bottom right left panels of Figure 6, we show that the hardness can be described by the square root of the observed flux, as is common for GRBs at higher energies observed with *BATSE* (e.g., Borgonovo & Ryde 2001; Ryde & Petrosian 2002; Kocevski, Ryde, & Liang 2003; Ryde 2005, Section 5).

For GRB 061121, the hardness plots show an initial hardening followed by a decrease in the hardness which scales well with the square root of the X-ray rate. There may be broad pulses on top of the decline, although these have only a minor impact on the hardness. GRB 060614 appears to mostly to exhibit a secular decline in both flux and hardness, corresponding to the fading tail of the prompt emission.

For each GRB, the hardness plot capture the  $E_{\text{peak}}$  evolution in general terms. Both ( $HR$  and  $E_{\text{peak}}$ ) decrease during rate declines at a similar power of the rate. It is apparently not possible to cleanly if at all separate evolution of  $\alpha$  from evolution of  $E_{\text{peak}}$ , given the hardness alone. From Figures 3 (top right) and 3 (middle right) and also from time-resolved spectral studies of many GRBs (Section 5), these parameters tend to evolve simultaneously.

#### 4. Example Spectra for 4 Other Early Afterglows

Most early X-ray afterglows have a low signal-to-noise or no coincident detection by the BAT. It is possible to derive  $E_{\text{peak}}$  values or limits for these early on, given the BAT data. Late time  $E_{\text{peak}}$  from the X-ray data typically show values in or passing through the XRT band after one to several minutes. The spectral evolution from one such event, GRB 060714 (Krimm et al. 2006), is shown in Figure 7.

The hardness plot (Figure 7 middle) allow for a finer time sampling of the spectra evolution. The hardness (likely also  $E_{\text{peak}}$ ) rises and declines with the flux along the same track in the hardness–rate plane as two flares take place. The column density (not plotted) is a factor two larger in the time interval 140–170s than outside that interval, indicating an

$E_{\text{peak}}$  passage. There are a handful of examples with higher signal-to-noise XRT observations.

The GRB 060526 (Campana et al. 2006b) afterglow exhibits time-correlated  $\Gamma$ – $N_H$  variations and a corresponding rapid then smooth decline of  $E_{\text{peak}}$  through the XRT band (Figure 8 left). The initial GRB pulse ( $t < 9.4\text{s}$ ) is well fit by a simple powerlaw ( $\alpha = -1.6 \pm 0.2$ ,  $\chi^2/\nu = 16.83/16$ ), and we derive  $E_{\text{peak}} > 80 \text{ keV}$  (90% confidence). The flare at  $t \sim 250\text{s}$  is detected by the BAT as well, and we use the BAT data to obtain the best Band model fits. The Band model photon indices are poorly measured. The composite flare and decline is shown in Figure 9. The hardness evolves similarly to the best-fit  $E_{\text{peak}}$  values.

The very bright afterglow to GRB 060729 (Grupe et al. 2006a) continues to be detected 4.5 months after the GRB. The GRB is over and done with by  $t \sim 130\text{s}$  in the BAT. We find  $E_{\text{peak}} > 50 \text{ keV}$  (90% confidence). After  $t > 100\text{s}$  in the XRT, there is a rapid decline, interrupted by a flare or rise at  $160\text{s}$  (Figure 9). Time-correlated  $N_H$ – $\Gamma$  variations and an  $E_{\text{peak}}$  passage through the X-ray band are similar to those discussed above (Figure 8). We observe that  $E_{\text{peak}}$  declines with the X-ray rate as  $F_{\text{XRT}}^{-0.4 \pm 0.1}$  both before and after the mild flare at  $t \sim 180\text{s}$ . There is also a possibly significant decline in  $\beta$  with time.

The hardness declines by an order of magnitude, reaching a minimum at  $t \sim 250\text{s}$ , and then increases to the late time ( $t > 10^3\text{s}$ ) value. Note that no clear coincident change is present in the rate plot. The hardness plot demonstrates that the late time emission is spectrally different from the early emission and that its onset occurs at  $t \sim 250\text{s}$ .

Modest but clear  $N_H$ – $\Gamma$  variations are seen for GRB 060904B (Grupe et al. 2006b). The prompt emission ( $t < 8.3\text{s}$ ) has  $E_{\text{peak}} = 125_{-30}^{+135} \text{ keV}$ .  $E_{\text{peak}}$  transits the X-ray band nicely (Figure 8). The hardness evolution shows the usual time dependence in the declining tail of the flare (Figure 9).  $E_{\text{peak}}$  decays versus the rate as  $F_{\text{XRT}}^{-0.7 \pm 0.2}$ .

The emission for GRB 060929 (Markwardt et al. 2006) at  $t < 13\text{s}$  exhibited  $E_{\text{peak}} > 75 \text{ keV}$ . The X-ray flare peaking at  $t \sim 550\text{s}$  is weakly detected by the BAT. In the XRT, there is a clear softening trend (Figure 9), likely  $N_H$ – $\Gamma$  variations, and an  $E_{\text{peak}}$  declining through the X-ray range (Figure 8).  $E_{\text{peak}}$  drops with the X-ray rate as  $F_{\text{XRT}}^{-0.6 \pm 0.1}$ . The hardness reaches a minimum at  $t = 630 \pm 10\text{s}$ .

## 5. Discussion

### 5.1. Global Sample Properties

In terms of the spectral evolution properties, we see no apparent difference between the fading tales of flare-like X-ray emission and the rapid X-ray declines often observed to trail

flaring in the BAT (e.g., Tagliaferri et al. 2005; Barthelmy et al. 2005; Cusumano et al. 2006; Vaughan et al. 2006). Indeed, based solely on timing properties, many of the rapid declines also appear to have superimposed flaring (e.g., 060729, Figure 9; 061121, Figure 6). The rapid declines are thought to be the fading tail of the prompt emission (Panaitescu et al. 2006; Yamazaki et al. 2006; Lazzati & Begelman 2006; Zhang et al. 2006), and the X-ray flares are thought to be due to later central engine activity (Zhang et al. 2006; Ioka et al. 2005; Fan & Wei 2005). We observe a clear distinctions between the spectra measured before the light curve plateau and after the start of the plateau; only the late spectra exhibit a tight clustering with  $\Gamma \approx 2$  (Figure 10; Paper I; Butler & Kocevski (2007)).

Figure 11 shows what we expect to measure from powerlaw fits to a time-evolving Band model spectrum. As  $E_{\text{peak}}$  enters the X-ray band, the spectral curvature as would be seen on a plot with logarithmic axes increases and the inferred X-ray column density increases linearly with an increasing inferred photon index  $\Gamma$ . This occurs despite the fact that only  $E_{\text{peak}}$  changes in the simulation. Figure 12 suggests that the effect is common in the XRT data (Section 5.2).

Figure 13 (left) shows that the flares (Table 2) and rapid X-ray declines exhibit significant hardness–intensity and hardness–fluence correlations which match closely the correlations observed for GRBs (Section 5.3 below).

For GRBs it is common to observe finer time structure at higher energies as compared to low energies (Norris et al. 1996; Fenimore et al. 1995; Fenimore, Madras, & Nayakshin 1996). Pulses tend to be narrower, fade more rapidly, and evolve stronger spectrally at high energies. Consistent with this, the X-ray flares (and also the rapid declines) appear longer ( $8 \pm 1\%$  on average, Figure 14 left) and with smoother time structure (e.g., Figure 2) at softer energies. This can be understood as the effect of  $E_{\text{peak}}$  evolving into the X-ray band, which allows the X-ray emission to be observed for longer (e.g., Kocevski, Ryde, & Liang 2003, and Section 5.4). Although it is difficult to see by a eye, there is also evidence for a  $25 \pm 5\%$  increase in the flare rise time with decreasing X-ray energy band (Figure 14 right). This is close to the expected pulse broadening fraction from an extrapolation of the GRB behaviour,  $1 - (1.3/0.5)^{-0.4} \approx 30\%$ , where 0.5 and 1.3 keV are used as approximate lower bandpass energies. Given the possibility that resolved  $\gamma$ -ray flares are blurred together in the X-ray band (e.g. Figure 2), however, it is not clear how meaningful this apparent consistency is.

## 5.2. The Physical X-ray Column Density Does Not Vary

The time-resolved XRT afterglows are well fit by absorbed powerlaws at all epochs (see also Paper I). Prior to a characteristic hardness variation turn-off time  $T_H \approx 10^2 - 10^4$ s, which we discuss for a large sample of bursts in (Butler & Kocevski 2007), there is strong evolution in both the best-fit photon indices and the best fit column densities  $N_H$ . After this time, the quantities typically do not vary. To fit more complicated models to the early time afterglows, we have found it necessary to jointly fit the BAT and XRT data (when possible) and to tie the column density to the value measured at late time. The late time value is typically not the Galactic value.

Band model fits are able to account for both the BAT and XRT emission without a time variable column density (see, also, Falcone et al. 2006). The ubiquitous hardness evolution appears to be best understood in terms of an evolving  $E_{\text{peak}}$ , as we discuss in detail below.

Several studies have claimed recently a decreasing  $N_H$  based on fits to the XRT data (Starling et al. 2005; Rol et al. 2006; Campana et al. 2006c, GRBs 050730, 050716, and 050904, respectively). Each study presents a coarsely time-resolved set of spectral fits, which demonstrate a higher  $N_H$  at early times. This is an artificial feature that we observe in fits to most *Swift* early afterglows. It is especially clear in the brightest afterglows, which often sample the declining tail of the prompt emission. For each of the 3 bursts with claimed  $N_H$  variations (e.g., Figure 15), a fine times-scale spectral analysis reveals an  $N_H$  which both increases and decreases in time (following  $\Gamma$  and the flux). Observed drops in  $N_H \gtrsim 10^{21}$  cm $^{-2}$  (or  $\gtrsim 10^{22}$  cm $^{-2}$  in the rest-frame) on timescales of 10 – 100s are challenging enough, but drops and increases and drops again on these timescales are unphysical.

We strongly caution against taking the early  $N_H$  values at face value. Measurements of  $N_H$  at  $t \lesssim 10^4$ s will be artificially high. Also, although we cannot rule variations out in all cases, they are not required by the data and they are also not the simplest interpretation of the data. Firm measurements of  $N_H$  variability will require finely time-sampled broadband data (e.g., Ultra-violet, X-ray, and  $\gamma$ -ray data) to disentangle the effects of the evolving Band model spectrum from the soft X-ray photoelectric absorption.

For those fitting XRT spectra, we recommend measuring  $N_H$  at late times ( $t \gtrsim 10^4$ s) or performing joint fits at different time intervals with a single  $N_H$  parameter shared between multiple spectra. Jointly fit with BAT when possible. Fine time resolution is essential when testing variable  $N_H$ ; it is not sufficient to fit exponential times powerlaw models or Band models (e.g., Rol et al. 2006; Campana et al. 2006c) with coarse time resolution. The hardness ratio can be utilized to diagnose cases where inferred  $N_H$  values are likely to vary artificially.

### 5.3. Is the Early XRT Emission the Same as Prompt GRB Emission?

We have shown for seven events that the early X-ray spectra require a fit model which also has been shown to reliably fit all GRBs (e.g., Preece et al. 2000; Kaneko et al. 2006; Frontera et al. 2000; Sakamoto et al. 2003). The need for such a model is also clear from hardness variations (see, also, Butler & Kocevski 2007) and time correlated  $N_H - \Gamma$  variations observed for even low signal-to-noise afterglows, which demonstrate a characteristic increase in spectral curvature in the XRT band.

In cases where  $E_{\text{peak}}$  is well measured, or using  $HR$  when  $E_{\text{peak}}$  is poorly measured, we observe a hard-to-soft evolution and a strong hardness–intensity correlation, also commonly seen in GRB pulses. Our correlation can be described as a hardness which tracks the flux to a power  $0.43 \pm 0.07$ . From the Band model fits, our best fit  $E_{\text{peak}} - F$  relation is  $0.7 \pm 0.2$  (Table 3). A closely consistent powerlaw relation exists for most GRB pulses, also with a large scatter in observed values (Golenetskii et al. 1983; Kargatis et al. 1995). The scatter is apparently minimized for bolometric measures of flux (Borgonovo & Ryde 2001), yielding  $E_{\text{peak}} \propto F_{\text{bol}}^{0.5 \pm 0.2}$ . The fact that we have observed a consistent relation can be turned around to imply GRB-like emission with  $E_{\text{peak}} \approx 1\text{keV}$ , typically. That *Swift* observes bright X-ray flares appears to be a consequence of this and also due to the surprising fact that the afterglow is faint at these times. It is interesting to speculate that there may be bright optical flares due to internal shocks at times of several hours after some GRBs with faint afterglows.

The typical  $E_{\text{peak}}$  values for the XRT are two orders of magnitude below the mode of the *BATSE* distribution (Preece et al. 2000; Kaneko et al. 2006). As we discuss below, some of the soft  $E_{\text{peak}}$  values may be due to viewing effects of delayed emission with an intrinsically higher  $E_{\text{peak}}$ . However, the soft flare emission implies intrinsic spectral evolution or soft late central engine activity which would extend the *BATSE*  $E_{\text{peak}}$  distribution. Our derived values for  $\alpha$  are poorly constrained, but likely consistent with the *BATSE* distribution. Finally, it is remarkable that very soft emission is observed in a few cases, extending the distribution in  $\beta$  to very low values  $< -6$  (Figures 8 and 10; GRBs 050714B and 050822 discussed in Paper I).

### 5.4. Interpretation of the Spectral Variations

Although intrinsic spectral evolution is likely also present, most of the softening trend and hardness–intensity correlation in GRB pulses is attributed to the so called “curvature effect” (Fenimore, Madras, & Nayakshin 1996; Sari & Piran 1997; Norris 2002; Ryde & Petrosian

2002; Kocevski, Ryde, & Liang 2003; Qin et al. 2004; Qin & Lu 2005; Shen, Song, & Li 2005). This is also the widely-accepted explanation for the rapid decline X-ray tails of the prompt emission (Nousek et al. 2006; Zhang et al. 2006; Panaiteescu 2007). Derivations from first principles of the curvature effect on the observed spectra can be found in Granot, Piran, & Sari (1999); Woods & Loeb (1999).

If we imagine a spherical emitting shell at radius  $R$  that emits as a delta function at  $t_o$ , the spectral flux  $F_E$  scales with the Doppler factor  $\delta$  as  $F_E \propto F_E[E\delta]/\delta^2$ . Here,  $\delta \equiv \gamma(1 - \beta_c \cos(\theta))/(1 - \beta_c) \approx 1 + \gamma^2\theta^2$ , where  $\theta$  is the viewing angle to emitting material off the line of site. The photons from larger angles will be delayed in time  $t - t_o = (1 + z)(\delta - 1)(1 - \beta_c)R/(c\beta_c) \approx (1 + z)\theta^2R/(2c) \propto \delta$ .

For a powerlaw spectrum  $F_E \propto E^{1-|\alpha|}$ , the observed flux declines in time as a powerlaw  $(t - t_o)^{-|b|}$ , with  $|b| = 1 + |\alpha|$  and no hardness evolution (Kumar & Panaiteescu 2000). For a Band spectrum, we see either the low energy index  $\alpha$  or the high energy index  $\beta$  or some average of the two, depending on the location of  $E_{\text{peak}}$  with respect to the bandpass.  $E_{\text{peak}}$  will decline as  $(t - t_o)^{-1}$ . When  $E_{\text{peak}}$  is in the band, the  $\nu F_\nu$  turnover implies  $-\alpha_{\text{eff}} \approx 1 - 2$ , and we expect to see a powerlaw hardness–intensity correlation  $E_{\text{peak}} \propto F^{0.3-0.5}$ . Larger values of the index are favored observationally, because they correspond to a higher flux. We will observe the hardness (which our simulations show to scale linearly with  $E_{\text{peak}}$  for a range of Band model parameters) to approximately linearly correlate with the fluence. Departures from this expected behavior will occur for emitting shells of different shape, for an inhomogeneous emitting surface, for non-instantaneous emission, or if intrinsic spectral evolution dominates. Also, the measured flux decay in time is a strong function of the assumed  $t_o$  (e.g., Liang et al. 2006).

Our best fit  $HR-F$  relation index (Figure 13) and our average  $E_{\text{peak}}-F$  relation relation index (Section 5.3; Table 3) are consistent with those expected in this simple picture. Spectral variations are not inconsistent with the curvature effect, as recently suggested by Zhang, Liang, & Zhang (2006). Rather, they facilitate a higher order test of the curvature effect, and allow us to confirm the curvature effect in way that shows the X-ray phenomenology to closely parallel the  $\gamma$ -ray phenomenology. Moreover, the scatter in our  $HR-F$  relation (Figure 13 left) is less than that found for time-index–energy index relations (Nousek et al. 2006; Panaiteescu 2007), which assume powerlaw X-ray spectra.

The mean time index for the  $E_{\text{peak}}$  decays in Table 3 is  $-1.4 \pm 0.6$ , consistent with unity. This indicates that our choice to associate  $t_o$  with the start of the flare or pulse is roughly correct, in agreement with the findings of Liang et al. (2006). Although we see evidence that later flares often have lower  $E_{\text{peak}}$  in the same event with multiple flares (e.g., Figure 3), we do not see a correlation between  $t_o$  in Table 3 and  $E_{\text{peak}}$  just after that time.

We have observed two cases of  $\alpha$  evolution (Figures 3 right) which accompanies the  $E_{\text{peak}}$  evolution. Due to the proximity of  $E_{\text{peak}}$  to the bottom of the XRT pass band and also due to the possibility of a modestly incorrectly measured  $N_H$ , these cases should be interpreted cautiously. This evolution, or that observed for  $\beta$  (Section 5.3) cannot be accounted for by the curvature effect and must be intrinsic.

In most cases, the X-ray light curve is simply declining early on (possibly with weak flaring superimposed), and we observe approximately secularly declining  $E_{\text{peak}}$  and  $HR$  values. In a handful of cases where multiple flares follow a GRB (e.g., Figure 6, 060124; and 7, 060714), the hardness tracks the flux both upward and downward. Because the brightest case (060124 in Figure 3 right) also shows upward and downward  $E_{\text{peak}}$  trends, we believe this behavior is likely responsible for the  $HR$  evolution. The parallel or overlapping tracks observed here for bursts with multiple flares on the  $HR$ – $F$  diagram is also seen for GRB pulses (Borgonovo & Ryde 2001).

## 6. Conclusions

We have measured the spectral evolution properties for GRBs and afterglows in the *Swift* sample, taken prior to and including GRB 061210. We have established similar spectral evolution properties between the X-ray emission coincident with two GRBs (060124 and 061121) and the X-ray emission in the rapid declines following several GRBs and in 27 flares occurring  $10^2 - 10^3$  after their GRBs.

Indirectly from absorbed powerlaw fits which show a time-variable  $N_H$  and directly from Band model fits, we have derived constraints on the  $\nu F_\nu$  spectrum peak energy  $E_{\text{peak}}$ . We observe this quantity to evolve in time and to typically cross the XRT bandpass during the early X-ray afterglow. Because the X-ray hardness changes little for Band spectra with  $E_{\text{peak}}$  outside the bandpass, the strong hardness variation we observe in >90% of *Swift* early afterglows (Butler & Kocevski 2007) imply  $E_{\text{peak}} \approx 1$  keV, typically. We observe this evolution in data taken in both the WT and PC modes (e.g., 050607 and 050714B) and following both long duration and short duration (e.g., 050724 and 051227) GRBs. The hardness ratio and  $E_{\text{peak}}$  values scale with the flux as would be expected from the relativistic viewing effects of an expanding fireball. This implies that the true variability timescale is *even shorter* than that measured from the observed flare durations.

Because the late flares are typically softer than the GRB emission, and because the Band model  $\alpha$  and  $\beta$  parameters also appear to evolve in some cases, there is likely an intrinsic evolution of the fireball. If the flares are due to shells moving out with lower bulk Lorentz

factor or at larger radii than for the prompt emission, we may expect to see differences in the time properties of flares observed at different epochs. This will be explored in a separate paper (Kocevski & Butler 2007). If the evolution is occurring on longer timescale at later times, when the sensitive XRT is observing, the early X-ray afterglows would provide a unique test-bed for theories explaining GRBs, the emission mechanisms, and possibly the progenitors. The internal shocks must be active after  $10^3$ s and must be able to produce emission with  $E_{\text{peak}} \approx 1$  keV and very soft  $\beta \lesssim -6$  (see, also, Zhang et al. 2006). Especially relevant to the Gamma-ray Large Area Telescope (GLAST), electrons energized by the X-ray flares may Compton upscatter photons at larger radii or in the external shock to the  $\gamma$ -rays (Kocevski et al. 2007).

N. R. B gratefully acknowledges support from a Townes Fellowship at U. C. Berkeley Space Sciences Laboratory and partial support from J. Bloom and A. Filippenko. D. K. acknowledges financial support through the NSF Astronomy & Astrophysics Postdoctoral Fellowships under award AST-0502502. This work was conducted under the auspices of a DOE SciDAC grant (DE-FC02-06ER41453), which provides support to J. Bloom’s group. Special thanks to the *Swift* team for impressively rapid public release and analysis of the XRT data. Thanks to J. Bloom and the U. C. Berkeley GRB team for comments on the manuscript and several useful conversations. We thank an anonymous referee for a very useful and critical reading of the manuscript.

## REFERENCES

Band, D. L., et al. 1993, ApJ, 413, 281  
Barthelmy, S. D., et al. 2005, Nature, 438, 994  
Borgonovo, L, & Ryde, F. 2001, ApJ, 548, 770  
Burrows, D. N., et al. 2005a, Science, 309, 1833  
Burrows, D. N., et al. 2005b, Space Sci. Rev., 120, 165  
Butler, N. R. 2007a, ApJ, 656, 1001 (Paper I)  
Butler, N. R. 2007b, AJ in press, astro-ph/0611031  
Butler, N. R., et al. 2007, in preparation  
Butler, N. R., & Kocevski, D. 2007, in preparation

Campana, S., et al. 2006, *Nature*, 442, 1008

Campana, S., et al. 2006b, *GCN* #5162

Campana, S., et al. 2006c, *ApJL Accepted*, *astro-ph/0611305*

Cusumano, G., et al. 2006, *Nature*, 440, 164

Dickey, J. M., & Lockman, F. J. 1990 *ARAA*, 28, 215

Fan, Y. Z., & Wei D. M. 2005, *MNRAS*, 364, L42

Falcone, A., et al. 2006, *ApJ*, 641, 1010

Fenimore, E. E., et al. 1995, *ApJ*, 448, L101

Fenimore, E. E., Madras, C. D., & Hayakshin, S. 1996, *ApJ*, 473, 998

Fishman, G. J., et al. 1989, in *Proc. GRO Science Workshop* (Greenbelt: NASA GSFC), 2-39

Ford, L. A., et al. 1995, *ApJ*, 439, 307

Frontera, F., et al. 2000, *ApJ*, 127, 59

Gehrels, N., et al. 2004, *ApJ*, 611, 1005

Gehrels, N., et al. 2006, *GCN* #5839

Golenetskii, S. V., et al. 1983, *Nature*, 306, 451

Granot, J., Piran, T., & Sari, R. 1999, *ApJ*, 513, 679

Grupe, D., et al. 2006a, *GCN* #5365

Grupe, D., et al. 2006b, *GCN* #5505

Holland, S. T., et al. 2006, *GCN* #4570

Ioka, K., et al. 2005, *ApJ*, 631, 429

Kaneko, Y., et al. 2006, *ApJS*, 166, 298

Kargatis, V. E., et al. 1995, *Ap&SS* 231, 177

Kocevski, D., Ryde, F., & Liang, E. 2003, *ApJ*, 596, 389

Kocevski, D., & Butler, N. R. 2007, in preparation

Kocevski, D., et al. 2007, in preparation

Krimm, H. A., et al. 2006, GCN #5311

Kumar, P., & Panaiteescu, A. 2000, ApJ, 541, L51

Lazzati, D., & Begelman, M. C. 2006, ApJ, 641, 972L

Liang, E., & Kargatis, V. 1996, Nature, 381, 49

Liang, E. W., et al. 2006, ApJ, 646, 351

O'Brien, D. P., et al. 2006, ApJ, 647, 1230

Markwardt, C. B., et al. 2006, GCN #5654

Morretti, A., et al. 2006, A&A, 451, 777

Norris, J. P., et al. 1996, ApJ, 459, 393

Norris, J. P., 2002, ApJ, 579, 386

Nousek, J. A., et al. 2006, ApJ, 642, 389

Pagani, C., et al. 2006, ApJ, 645, 1315

Page, K. L., et al. 2006, GCN #5823

Painetescu, A., et al. 2006, MNRAS, 366, 1357

Painetescu, A. 2007, MNRAS submitted, astro-ph/0612170

Parsons, A. M., et al. 2006, GCN #5252

Preece, R. D., et al. 2000, ApJ, 126, 19S

Protassov, R., et al. 2002, ApJ, 571, 545

Qin, Y.-P., et al. 2004, ApJ, 617, 439

Qin, Y.-P., & Lu, R. J. 2005, MNRAS, 362, 1085

Rees, M. J., & Mészáros, P. 1994, ApJ, 430, L93

Rol, E., et al. 2006, MNRAS Accepted, astro-ph/0611554

Romano, P., et al. 2006a, A&A, 450, 59

Romano, P., et al. 2006a, A&A, 456, 917

Ryde, F., & Petrosian, V. 2002, ApJ, 578, 290

Ryde, F. 2005, A&A, 429, 869

Sakamoto, T., et al. 2003, ApJ, 602, 875

Sari, P., & Piran, T. 1997, ApJ, 485, 270

Sari, R., Piran, T., & Narayan, R. 1998, ApJ, 497, L17

Scargle, J. D. 1998, ApJ, 504, 405S

Shen, R. F., Song, L. M., & Li, Z. 2005, MNRAS, 362, 59

Starling, R. L. C., et al. 2005, A&A, 442, 21

Tagliaferri, G., et al. 2005, Nature, 436, 985

Vaughan, S., et al. 2006, ApJ, 638, 920

Willingale, R., et al. 2006, astro-ph/0612031

Wijers, R. A. M. J., & Galama, T. J. 1999, ApJ, 523, 177

Woods, E., & Loeb, A. 1999, ApJ, 523, 187

Yamazaki, R., et al. 2006, MNRAS, 369, 311

Zhang, B., et al. 2006, ApJ, 642, 354

Zhang, B.-B., Liang, E. W., & Zhang, B. 2006, astro-ph/0612246

Table 2: 27 Bright XRT Flares

GRB	Time Region [s]	GRB	Time Region [s]
050502B	400–1200	050712	150–300
050730	130–300	050730	300–600
050730	600–800	050822	410–650
050904	350–600	051117A	1250–1725
051117A	800–1250	060111A	200–500
060124	300–650	060124	650–900
060204B	100–270	060204B	270–450
060210	100–165	060210	165–300
060210	350–450	060418	83–110
060607A	93–130	060607A	220–400
060714	100–125	060714	125–160
060714	160–230	060729	156–300
060904A	250–600	060904A	600–1000
060904B	140–300		

Table 3:  $E_{\text{peak}}$  Evolution Properties

GRB	$t_{\text{o}}$ [s]	Time Index	Flux Index	Data Points	Fit
060124	510	$-2.9 \pm 1.3$	$-3.6 \pm 1.7$	2	
060124	555	$-2.2 \pm 0.3$	$-1.8 \pm 0.5$	3	
060124	567	$-0.8 \pm 0.1$	$-0.3 \pm 0.1$	4	
060124	685	$-2.2 \pm 0.4$	$-1.2 \pm 0.2$	3	
060526	240	$-1.2 \pm 0.1$	$-1.0 \pm 0.1$	5	
060614	0	$-2.1 \pm 0.1$	$-0.72 \pm 0.03$	19	
060729	75	$-2.0 \pm 0.5$	$-0.4 \pm 0.1$	5	
060729	155	$-0.7 \pm 0.2$	$-0.4 \pm 0.1$	4	
060904B	140	$-1.3 \pm 0.3$	$-0.7 \pm 0.2$	5	
060929	470	$-1.1 \pm 0.2$	$-0.6 \pm 0.1$	7	

Notes: Changes in the best-fit  $E_{\text{peak}}$  with time are relative to the start  $t_{\text{o}}$ . The start time is somewhat arbitrary, based on the approximate start of each pulse (or flare).

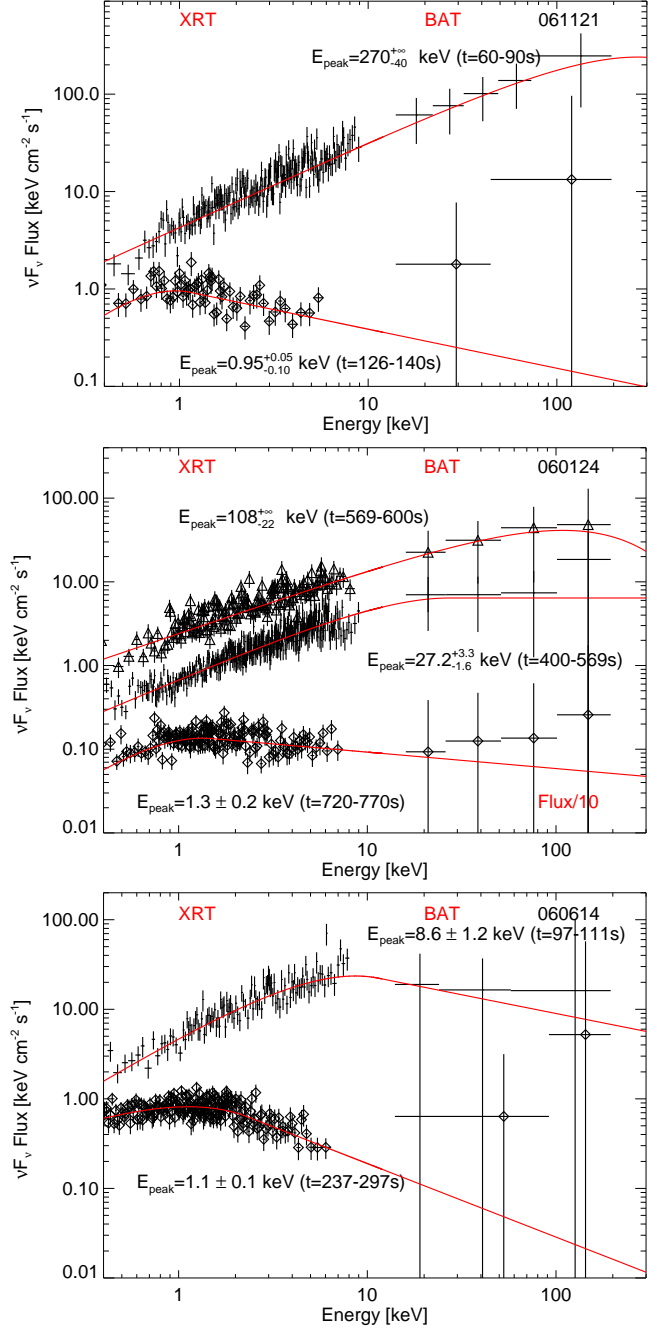


Fig. 1.— Selected  $\nu F_\nu$  spectra from GRBs 061121, 060124, and 060614, demonstrating the Band model fits to a time varying spectral curvature — as seen in plots with logarithmic axes — and  $E_{\text{peak}}$  evolution. The X-ray data are corrected for photoelectric absorption using the best fit late-time values of  $N_H$  in Figures 3 (left). The softest spectrum in the middle panel is divided by a factor ten for legibility. The counts spectra are jointly fit by forward folding the Band model through the instrument response matrices. For the spectral fits (Table 1), the BAT data are not binned as shown here.

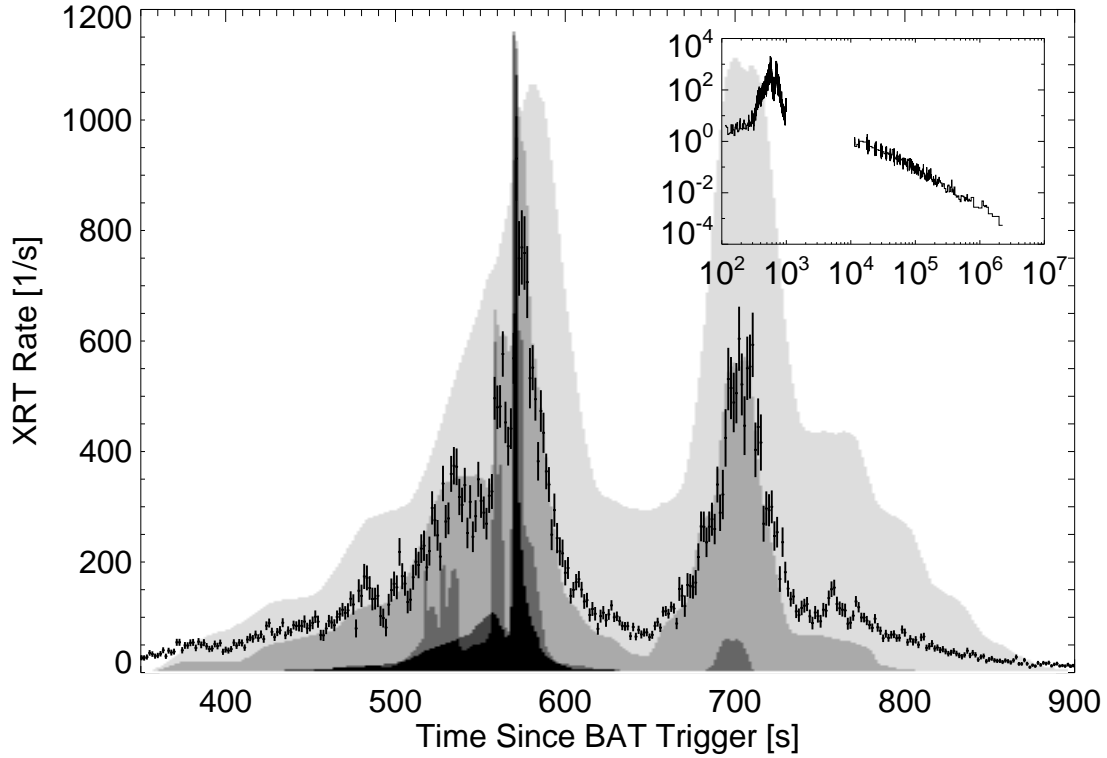


Fig. 2.— The light curve for GRB 060124. The X-ray data (0.3–10.0 keV) are plotted in black. The shaded regions in the background depict the X-ray light curves in two energy bands (0.3–1.3 keV and 1.3–10.0 keV) and in the hard X-ray/γ-ray bands of BAT (15–100 keV and 100–350 keV). The background light curves are each denoised and normalized to their peak intensity. The harder regions are darker. The sub-panel shows the early and late XRT light curve.

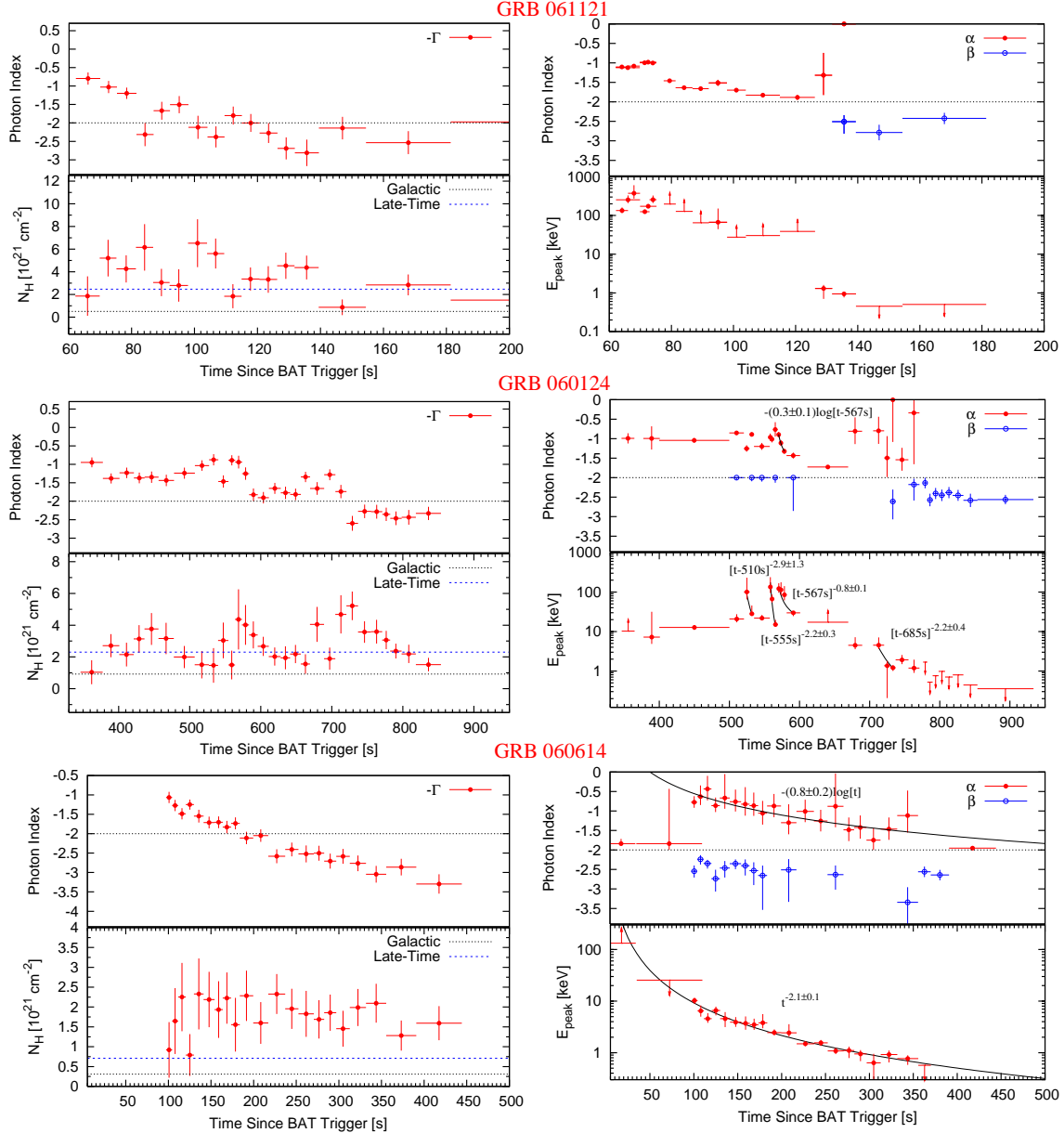


Fig. 3.— Powerlaw (left panels) and Band model (right panels) fits to the GRBs 061121, 060124, and 060614. Time-correlated  $N_H$ – $\Gamma$  variations in the left plots are better modelled by spectral models with time-evolving  $E_{\text{peak}}$ ’s in the right plots. The  $N_H$  values peak when  $E_{\text{peak}} \approx 1$  keV. The powerlaw fits are performed for only the X-ray data, whereas the Band fits (actually nested powerlaw then exponential times powerlaw then Band fits, as described in the text) apply to the X-ray and  $\gamma$ -ray data. Trends in the Band model parameters, when observed, are fitted and presented in Table 3 and in the text. These time variations are given relative to the approximate pulse start times. Galactic column densities are taken from Dickey & Lockman (1990) The Band fits use the late time  $N_H$  values plotted in the left panels, derived from X-ray fits at  $t > 10^4$  s.

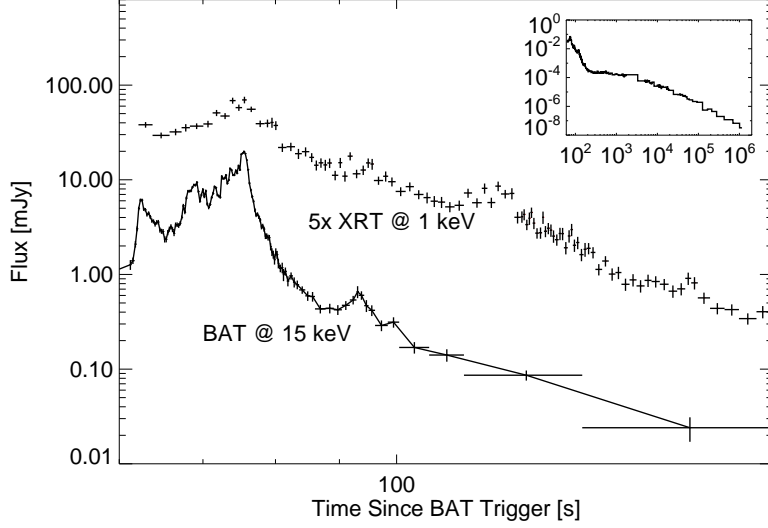


Fig. 4.— The hard X-ray BAT and XRT light curves for GRB 061121. The late-time light curve (a plateau at  $t \sim 200$ s followed by a decline beginning at  $t \sim 3000$ s) is plotted in the sub-panel. The XRT light curve has been multiplied by 5 to bring it above the BAT light curve.

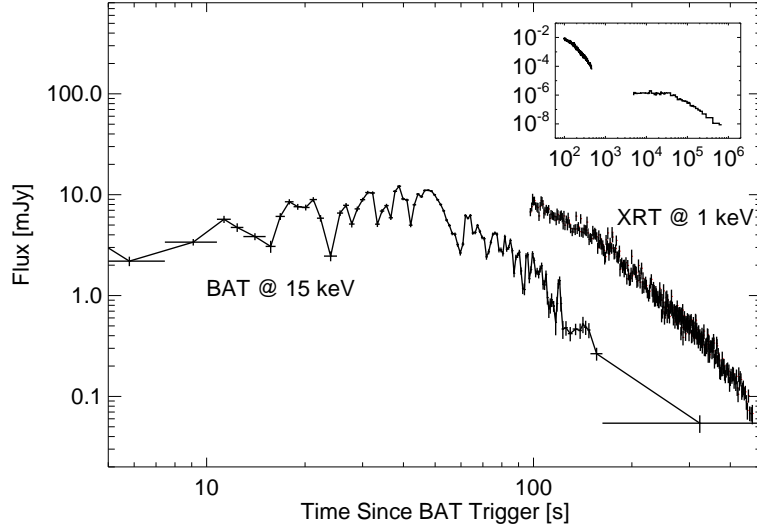


Fig. 5.— The hard X-ray BAT and XRT light curves for GRB 060614. The late-time light curve (a plateau at  $t \sim 200$ s followed by a decline beginning at  $t \sim 4000$ s) is plotted in the sub-panel.

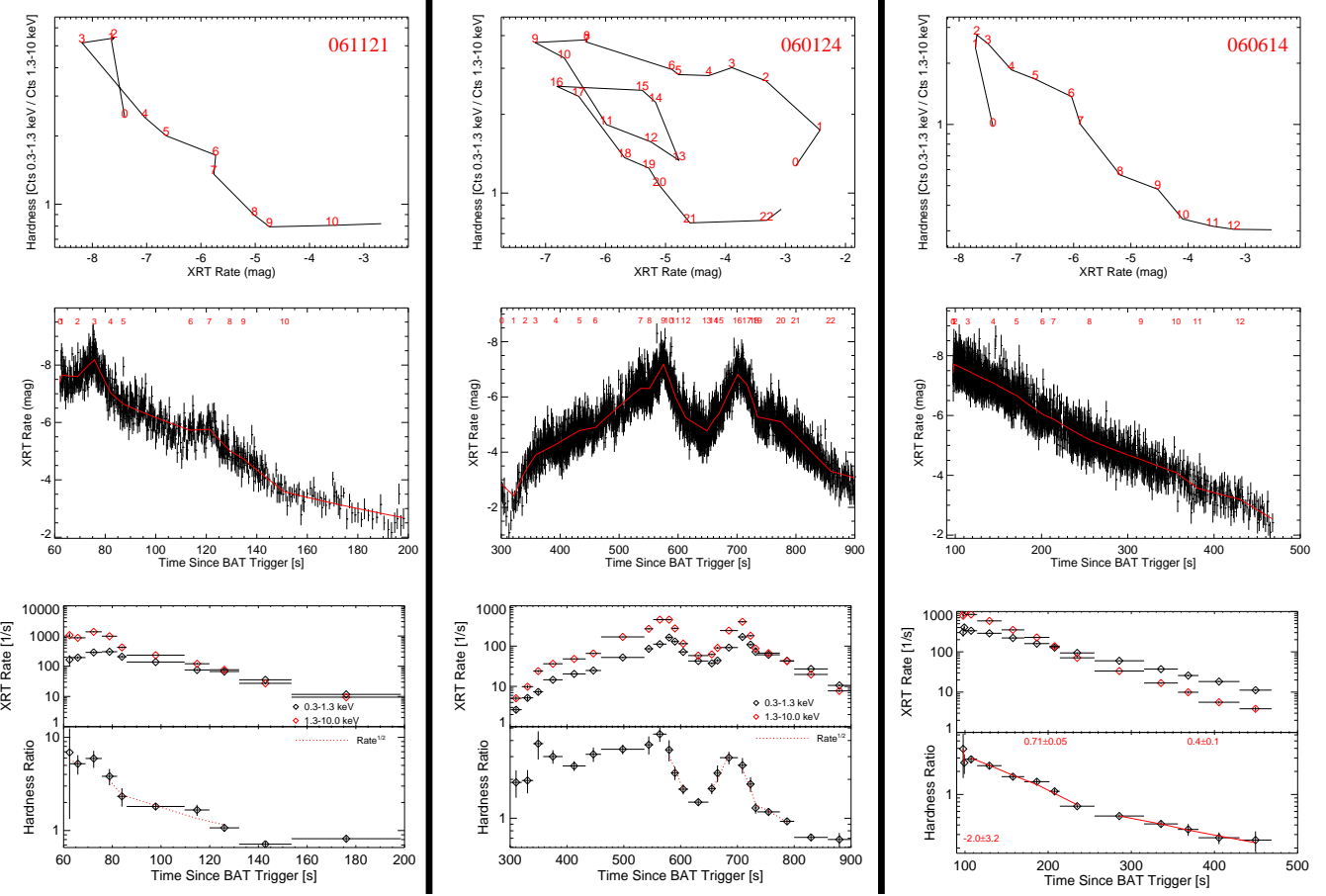


Fig. 6.— The hardness evolution in GRBs 061121, 060124, and 060614. (top plots) Hardness versus rate fit, indexed as a function of time, showing evolution along roughly parallel tracks. (middle plots) The X-ray light curve and fit (red curve) as source of the time indexing. (bottom plots) The X-ray light curve in each band (hard is red, soft is black) for each time segment and the hardness during each time segment. This is well fit during the declines by the square-root of the rate (dotted red line) in GRBs 061121 and 060124 and by a power close to the square root of the rate for GRB 060614.

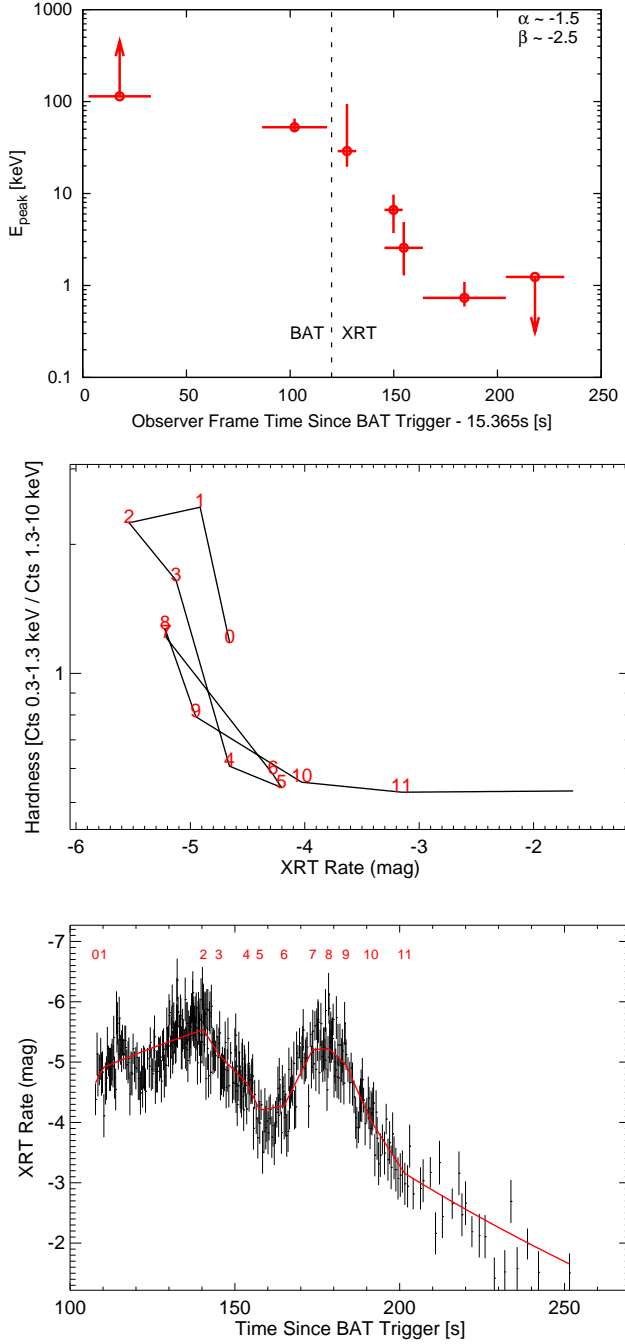


Fig. 7.— Plots of the hardness and  $E_{\text{peak}}$  evolution for flares after GRB 060714. The Band fits allow only a coarse time resolution, whereas the hardness study demonstrates a fine timescale changes in the spectrum which track the flux across flares.  $E_{\text{peak}}$  evolution from Band model fits to the BAT and XRT data (top plot). Typical values for the photon indices ( $\alpha, \beta$ ) are given. Hardness versus rate fit (middle and bottom plots), indexed as a function of time, showing parallel evolution tracks.

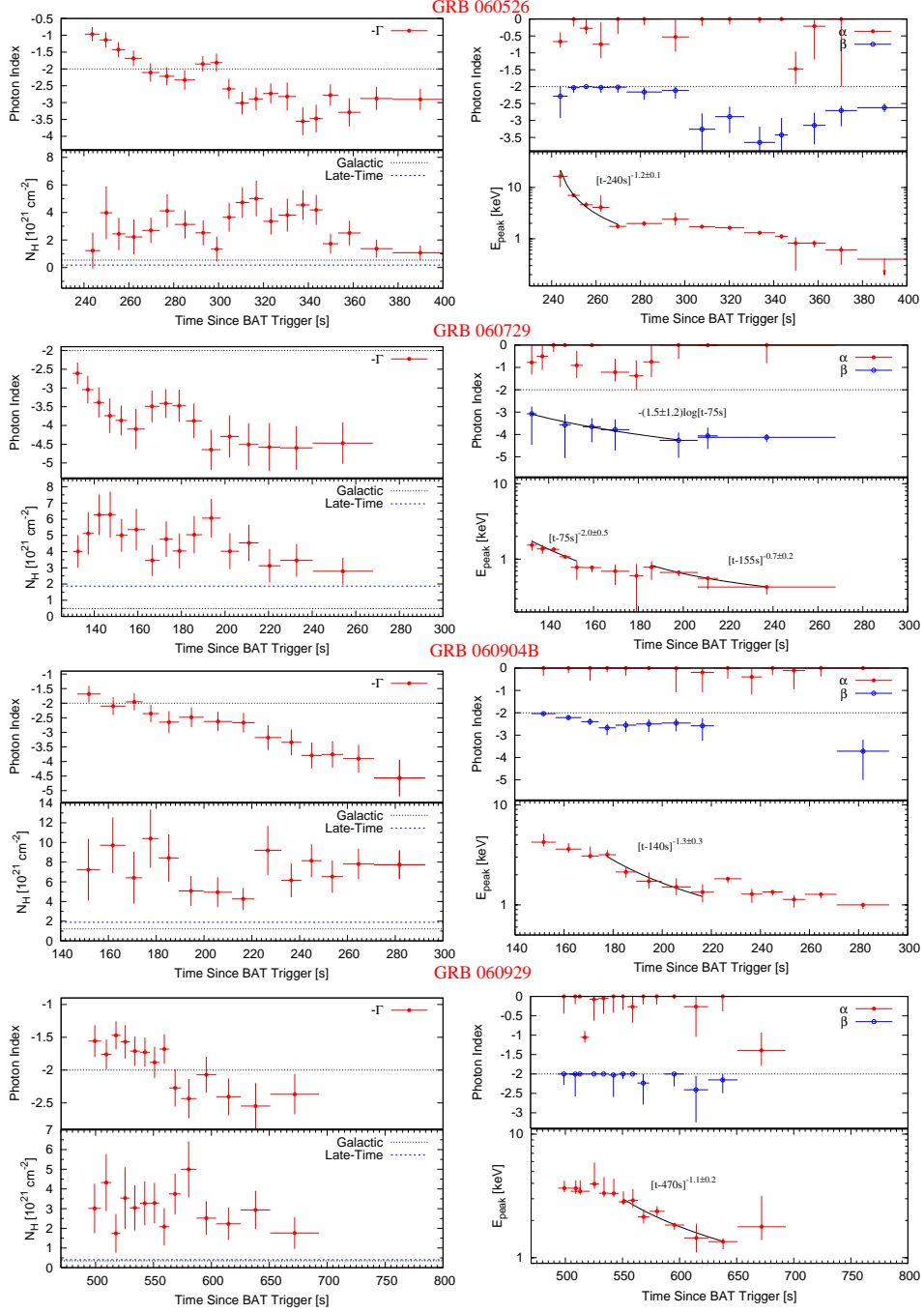


Fig. 8.— Powerlaw (left panels) and Band model (right panels) fits to the GRBs 060526, 060729, 060904B, and 060929. Time-correlated  $N_H$ – $\Gamma$  variations in the left plots are fit by spectral models with time-evolving  $E_{\text{peak}}$ 's in the right plots. Trends in the Band model parameters, when observed, are fitted and presented in Table 3 and in the text. See also Figure 3. In the Band model plots,  $\alpha$  values which appear to be above and outside of the plotted range are those which reach and remain at the parameter bound  $\alpha = 0$  (see Section 3.1).

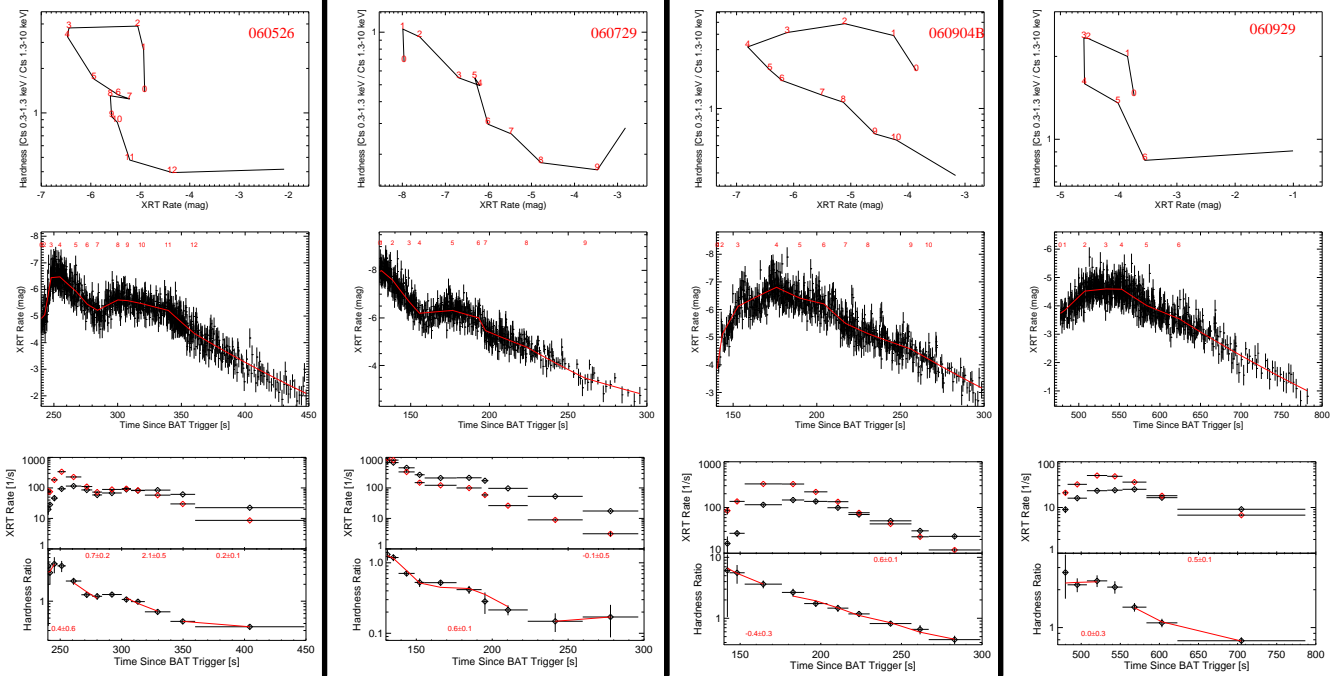


Fig. 9.— Hardness plots for GRBs 060526, 060729, 060904B, and 060929. (top plots) Hardness versus rate fits, indexed as a function of time, showing evolution along roughly parallel tracks. (middle plots) The X-ray light curve and fit (red curve) as source of the time indexing. (bottom plots) The X-ray light curve in each band (hard is red, soft is black) for each time segment and the hardness during each time segment. This hardness is well fit during the declines by the rate to a power close to 0.5 (dotted red curves). See also Figure 6.

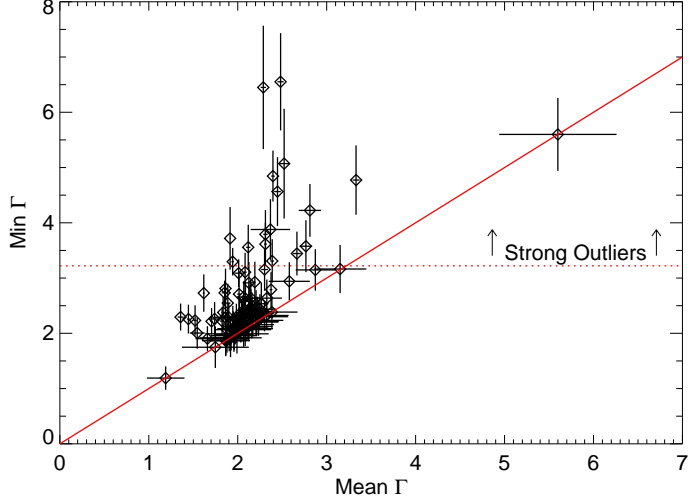


Fig. 10.— As also discussed in Paper I, there is an outlier population of very soft *Swift* XRT afterglow time regions with respect to the majority population clustering near photon index  $\Gamma \sim 2$ .

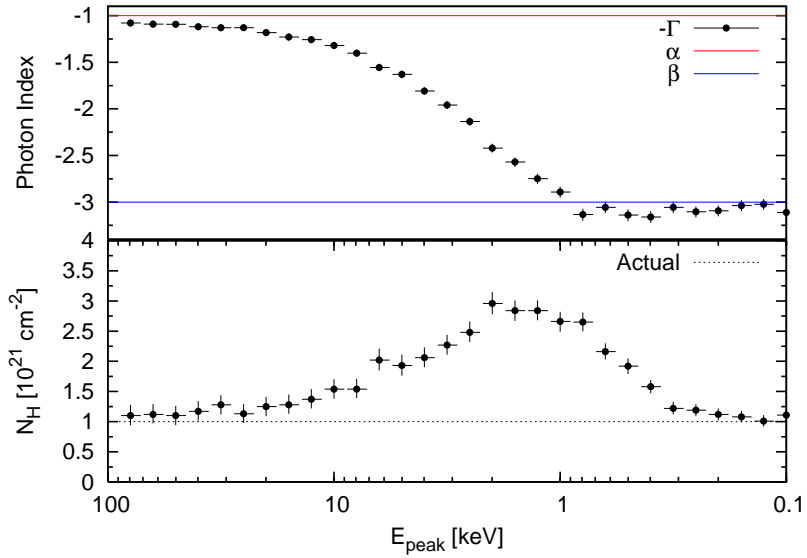


Fig. 11.— Powerlaw fits to high signal-to-noise data ( $10^4$  counts, 0.3–10.0 keV) simulated from a Band spectral model with  $\alpha = -1$  and  $\beta = -3$ . Each fit is statistically acceptable ( $\chi^2/\nu \sim 1$ ). With the passage of the  $\nu F_\nu$  peak energy  $E_{\text{peak}}$ , the best-fit photon index  $\Gamma$  steepens smoothly. An artificial increase in the inferred X-ray column density  $N_H$  linearly proportional to  $\Gamma$  is observed for peak energies  $E_{\text{peak}}$  in the XRT bandpass. The effect is present, with larger  $N_H$  error bars, for spectra with few counts.

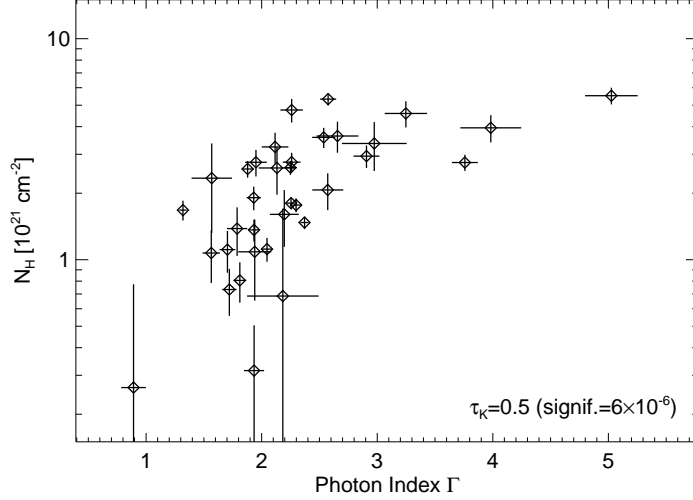


Fig. 12.— Time integrated spectral fits to the flares in Table 2, also shown in Figure 13, demonstrate a significant positive correlation between the column density parameter  $N_H$  (observed minus Galactic) and the photon index  $\Gamma$ . Although these quantities are correlated for a given spectrum, we do not expect a correlation at different times for the same event (see below) or at any time for separate events as found here. This is evidence tying the X-ray flares to an excess spectral curvature at X-ray wavelengths.

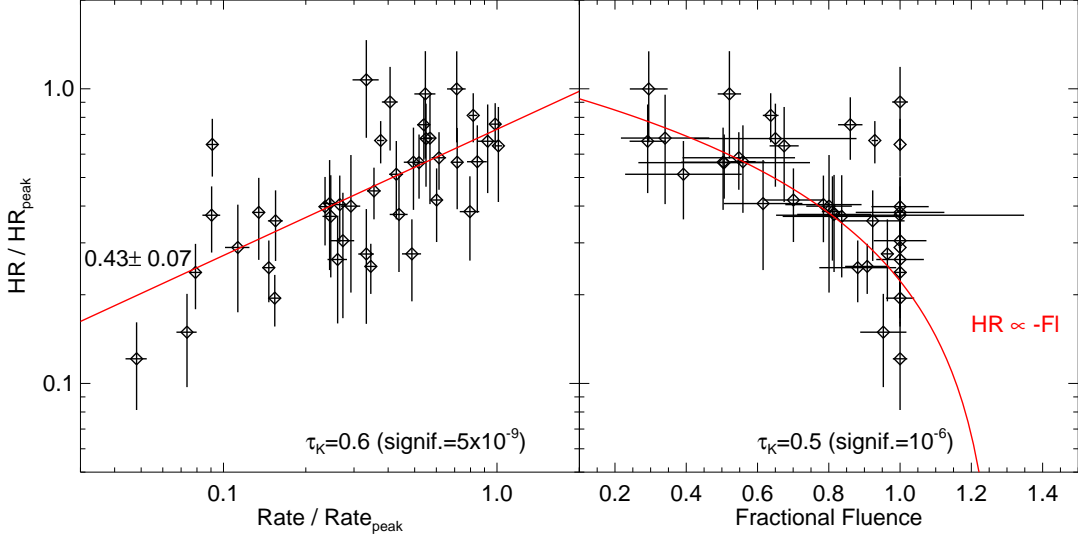


Fig. 13.— During the decline phase of the X-ray flares from Table 2 (also Figure 12), the hardness ratio ( $HR$ ), defined as the ratio of counts in the 1.3–10.0 keV band to the counts in the 0.3–1.3 keV band, correlates strongly (Kendall’s  $\tau_K = 0.6$ ) with the count rate (0.3–10.0 keV), following roughly a powerlaw relationship (left plot). There is a consistent and long known relation valid for a majority of pulses seen in GRBs (Golenetskii et al. 1983; Kargatis et al. 1995; Ford et al. 1995; Borgonovo & Ryde 2001). The hardness also correlates strongly with the fluence (right plot), as is also the case for GRBs (Liang & Kargatis 1996; Ryde 2005). That is, the hardness evolves more rapidly when the flares are brighter.

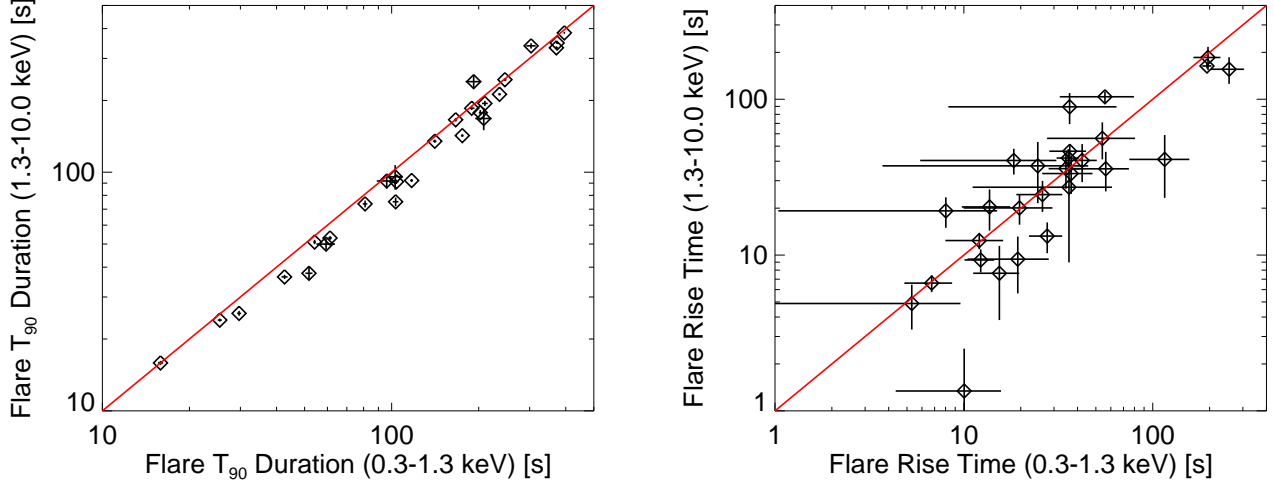


Fig. 14.— Timing statistics for the bright flares in (Table 2). The flare  $T_{90}$  durations (left plot) and rise times (right plot) are systematically longer in the soft X-ray channel (left plot), by  $8 \pm 1\%$  and  $25 \pm 5\%$ , respectively. Norris et al. (1996); Fenimore et al. (1995); Fenimore, Madras, & Nayakshin (1996) discuss similar properties of GRB pulses.

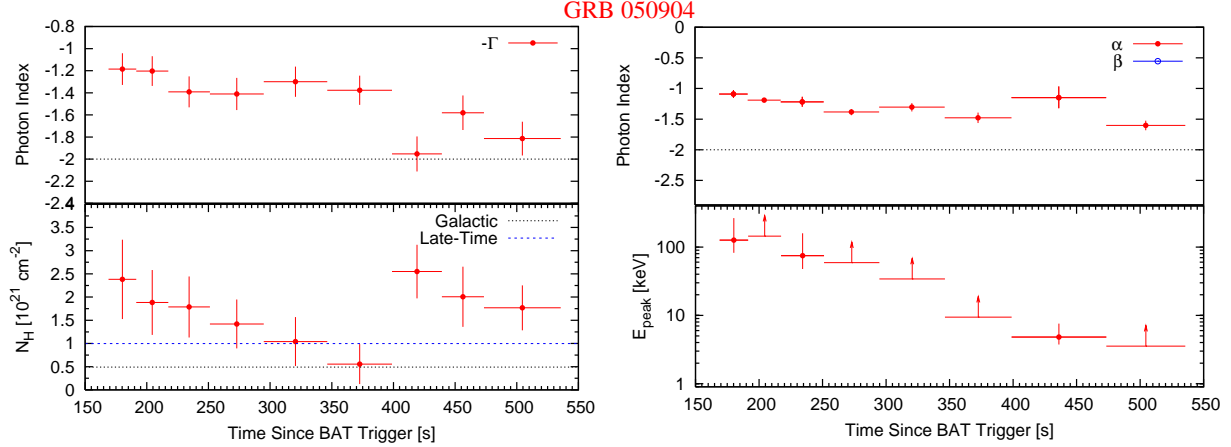


Fig. 15.— We believe  $N_H$  variations are an incorrect explanation for the spectral evolution in the flaring, high- $z$  GRB 050904. These data are coarsely grouped into three time intervals by Campana et al. (2006c) and fit to show a time-decreasing X-ray column density. At finer time resolution (left plot), we see that the  $N_H$  parameter decreases toward the late time value before and after an unphysical increase. The maximum  $N_H$  corresponds to  $E_{\text{peak}}$  in the XRT band (right plot). The hardness during this period tracks the flux to the  $0.6 \pm 0.2$  power (see also, Figure X in Butler & Kocevski 2007b), consistent with a Band model spectrum evolving via the curvature-effect (Section 5.4).

Table 1. Selected Band or Powerlaw\*Exponential Model Spectral Fits

GRB	Time	$\alpha$	$\beta$	$E_{\text{peak}}$	0.3-10 keV Flux	$\chi^2_{\nu} (\nu)$	Signif.
	[s]			[keV]	[ $10^{-9}$ erg cm $^{-2}$ s $^{-1}$ ]		
060124	569–600	$-1.23 \pm 0.04$	...	$108^{+\infty}_{-22}$	$26.8 \pm 1.0$	1.21 (154)	$5.9\sigma$
060124	400–569	$-1.04 \pm 0.03$	$-2.0^{+0.0}_{-0.1}$	$27.2^{+3.3}_{-1.6}$	$8.6^{+0.2}_{-0.1}$	1.01 (410)	$10^{-77}$
060124	720–770	$-0.3^{+0.3}_{-0.6}$	$-2.2 \pm 0.1$	$1.3 \pm 0.2$	$5.8^{+0.3}_{-0.2}$	1.08 (158)	$10^{-12}$
061121	60–90	$-1.12^{+0.01}_{-0.02}$	...	$270^{+\infty}_{-40}$	$55.3^{+1.0}_{-1.3}$	1.07 (270)	$9.3\sigma$
061121	126–140	$-0.0^{+0.0}_{-0.9}$	$-2.4^{+0.1}_{-0.2}$	$0.95^{+0.05}_{-1.0}$	$3.7 \pm 0.2$	1.16 (117)	$3.9\sigma$
060614	97–111	$-0.7 \pm 0.1$	$-2.4 \pm 0.1$	$8.6 \pm 1.2$	$59^{+3}_{-2}$	0.86 (169)	$10^{-98}$
060614	237–297	$-1.2 \pm 0.2$	$-2.8^{+0.2}_{-0.3}$	$1.1 \pm 0.1$	$3.2 \pm 0.1$	0.97 (246)	$10^{-27}$

Note.—The quoted errors correspond to the 90% confidence region. The “Signif.” column refers to the fit improvement significance relative to a simple powerlaw model, determined from a  $\Delta\chi^2$  test. The quoted fluxes are unabsorbed.